A nonlinear resonator with inertial amplification for very low-frequency flexural wave attenuations in beams

Jiaxi Zhou [*a], Lingling Dou [a], Kai Wang [a], Daolin Xu [a, b], Huajiang Ouyang [c]

[a] *College of Mechanical and Vehicle Engineering, Hunan University, Changsha 410082, PR China,*

[b] *State Key Laboratory of Advanced Design and Manufacturing for Vehicle Body Changsha 410082, PR China,*

[c] *School of Engineering, University of Liverpool, Liverpool L69 3GH, UK*

Abstract

Although elastic metamaterials in a subwavelength scale can control macroscopic waves, it is still a big challenge to attenuate elastic waves at very low frequency (a few tens Hz). The main contribution of this paper is to develop a high-static-low-dynamic-stiffness (HSLDS) resonator with an inertial amplification mechanism (IAM), which is able to create a much lower band gap than a pure HSLDS resonator. The nonlinear characteristics of a locally resonant (LR) beam attached with such new resonators are also explored. The band gap of this LR-IAM beam is revealed by employing transfer matrix method and validated by numerical simulations using Galerkin discretization. It is shown that a very low-frequency band gap can be formed by tuning the net stiffness of the resonator towards an ultra-low value. In addition, the nonlinearity, arising from the restoring force of the resonator, the damping force and effective inertia of the IAM, gives rise to an intriguing feature of amplitude-dependent wave attenuation, which could potentially act as a switch or filter to manipulate flexural waves.

Keywords: wave attenuation, low frequency, local resonance, inertial amplification, nonlinearity.

[*] Corresponding author.
College of Mechanical and Vehicle Engineering, Hunan University, Changsha 410082, PR China.
E-mail address: jxizhou@hnu.edu.cn (Jiaxi Zhou). Telephone number:+86 13975835883

1. Introduction

The radiated noise emitted from the machines onboard an underwater vehicle is detrimental to its acoustic stealth, especially when it is in low speed navigation [1]. In such a case, the main contributions to the radiated noise can be ascribed to the low-frequency vibrations arising from the machines and propagating along the raft and the hull. Hence, it is essential to attenuate the vibrations and prevent them from propagating along structures. Beside the common method of vibration isolation [2-4] for this issue, another potential solution is to exploit a periodic structure to engineer phononic crystals [5] or locally resonant (LR) metamaterials [6]. Especially, the LR metamaterials are capable of mitigating wave propagation at low-frequency regime, due to their intriguing feature of deep subwavelength [6, 7].

Acoustic (elastic) metamaterials, man-made materials with unprecedented wave manipulation functions, have drawn more and more attention. The past nearly two decades have witnessed a surge on conceptual designs, theoretical studies and potential applications of acoustic (elastic) metamaterials, which has been well documented in the comprehensive review papers [7-9]. Fok et al [6] divided acoustic metamaterials into two types: the intrinsic and inertial ones. This paper mainly focuses on the latter realized by embedding local resonators into the elastic matrix for attenuating low-frequency waves.

The first work on the LR metamaterials was carried out by Liu et al [10], where heavy spheres coated with soft silicon rubber were embedded into epoxy matrix. Such constituent components act as mass-spring resonators so as to exhibit a band gap at a frequency well below that arising from Bragg scattering, due to spatially periodic impedance mismatch. This broke a reliance on the lattice constant of Bragg scattering band gap, and opened a new mechanism to create a low-frequency band gap by employing a small sample that is deep-subwavelength at resonant frequencies [6]. A

beam with periodically suspended masses is a common category of LR metamaterials for manipulating flexural waves. Yu et al. [11] proposed an LR beam with resonators constituting of a soft rubber ring and a copper ring, and Yu et al. [12] also studied the propagation properties of flexural waves in an LR beam on an elastic foundation. Xiao et al. [13] studied the formation mechanism of band structures in LR beams theoretically, and obtained the analytical expressions of the bound frequencies of the band gap. Liu and Hussein [14] studied the transition criterion between Bragg scattering and local resonance for an LR beam. Zhu et al. [15] constructed a chiral metamaterial beam for vibration suppression.

As well-known, the LR band gap has an intrinsic characteristic of narrow bandwidth. To broaden the band gap, Wang et al. [16] proposed a continuum-beam resonator, and Xiao et al. [17] suggested using multiple periodic arrays of oscillators with distributed resonant frequencies in one unit cell, which can merge multiple narrow band gaps into a wide one [18]. Chen et al. [19] periodically attached shunted piezoelectric patches onto host beams as tunable resonators for broadband flexural wave manipulations. Alternatively, the inertial amplification mechanism (IAM) [20-28] is also an important way to create low and wide band gaps. Yilmaz et al. [20, 21] first proposed the method of inertial amplification, which also was validated by experimental tests [22], and several novel inertial amplification mechanisms were achieved via design optimization [23, 24]. Frandsen et al. [25] proposed to use inertial amplification to generate band gaps in continuous structures by attaching light-weight IAM, and Barys et al. [26] realized this concept for flexural wave attenuation in a beam. Li and Li [27] also periodically attached IAMs onto an elastic beam to generate wide low-frequency band gap. Hou et al. [28] proposed beam-like inertial amplification metamaterials to obtain ultra-low frequency band gap.

However, as mentioned in Ref [8], it is still a great challenge to achieve an ultralow-frequency band gap, due to the fact that it is almost impossible to substantially reduce the resonant frequency by making the mass of the resonator

ultra-large and the stiffness ultra-low. Additionally, the vibrations or waves from mechanical machines are usually dominated by low-frequency components from 1 Hz to a few tens Hz. To resolve this tough issue, a high-static-low-dynamic-stiffness (HSLDS) resonator has been proposed in our previous works [29, 30], which indicated that a negative-stiffness mechanism introduced into the resonator could effectively neutralize the originally positive stiffness of the resonator, leading to ultra-low dynamic stiffness, while the ability of supporting the mass of the resonator remains unchanged. Consequently, a much lower-frequency band gap was realized by employing such HSLDS resonators than the conventional ones.

Furthermore, the stiffness of the HSLDS resonator is intrinsically nonlinear. As the amplitude of the excitation is increased, the nonlinearity would become too significant to be ignored, which could induce complicated behaviour of waves propagation in the phononic materials and acoustic (elastic) metamaterials, such as localization [31], breather [32], bifurcation [33] and chaos [34]. All of these phenomena were proved to be useful when manipulating waves for special functions. Vakakis et al. [31] studied a periodic chain of nonlinearly coupled oscillators under external excitations, which presented profound localized responses in the chain. Chakraborty and Malik [35] mainly focused on the nonlinear natural frequencies and the corresponding normal modes of the periodic chain considering both the hardening and softening types of nonlinearity. Narisetti et al. [36] gave an approximate close-form dispersion relation of the wave propagation in one-dimensional periodic structures, which exhibited a tunable band gap that shifts with wave amplitude. For the same system, Manktelow et al. [37] presented the interaction of two waves giving rise to different amplitude and frequency dependent dispersion relations. Boechler et al. [33] demonstrated a new mechanism for tunable rectification based on bifurcation and chaos in a granular chain with a defect (a lighter mass) near the boundary. However, the reports on the nonlinear LR metamaterials are rare in comparison with nonlinear periodic chain. Lazarov and Jensen [38] studied the wave propagation in a one-dimensional chain with attached nonlinear local resonators, which revealed the amplitude-dependent

dispersion and low-frequency band gaps. Fang et al. [34] reported a new chaos mechanism for ultra-low and ultra-broad band gaps in nonlinear LR metamaterials, which was realized by utilizing the strong nonlinearity arising from vibro-impact.

The aim of this paper is to substantially reduce the central frequency of the band gap of an HSLDS resonator by introducing an inertial amplification mechanism (IAM). The dynamic feature of the resonator with the IAM is analysed to reveal the principle for magnifying the overall inertia of the resonator. And the dispersion of the beam with inertially amplified resonators (called LR-IAM beam for short) is obtained using the transfer matrix method to demonstrate the band structure, where one can see the effectiveness of the IAM for forming a very low-frequency band gap. The other contribution of this paper is to explore the nonlinear dynamic characteristics of the LR-IAM beam. The approximate analytical amplitude-frequency relationships are obtained by using the harmonic balance method, where one can observe the multi-value feature of the responses. Global bifurcations with respect to the amplitude of excitation are determined numerically to show an interesting phenomenon of amplitude-dependent wave attenuation in the band gap.

The remainder of this paper is organized as follows. Section 2 shows how the IAM works, and presents the dispersion relations and band structures of the LR beam with HSLDS resonators containing the IAM. In section 3, the investigations on the wave attenuation characteristics of the LR-IAM beam are carried out numerically, when the actual nonlinear restoring forces, damping forces and effective inertia are considered. The nonlinear dynamic analysis, including multi-value responses and global bifurcations, are also conducted. Finally, some conclusions are drawn in Section 4.

2. Band gaps of LR-IAM Beams

Consider elastic wave propagating in an Euler-Bernoulli beam. In order to attenuate

low-frequency waves, the high-static-low-dynamic-stiffness (HSLDS) local resonators are periodically attached onto the beam, as shown in Fig. 1a. The resonator proposed here is to attach an additional inertia amplification mechanism (IAM) into the HSLDS resonator [29] to further lower the central frequency of the band gap, as depicted in Fig. 1b. The computational models of the LR-IAM beam and the resonator are illustrated in Fig. 1c and Fig. 1d, respectively. In this section, the stiffness characteristics are presented firstly, and then the band gaps are revealed by using transfer matrix method.

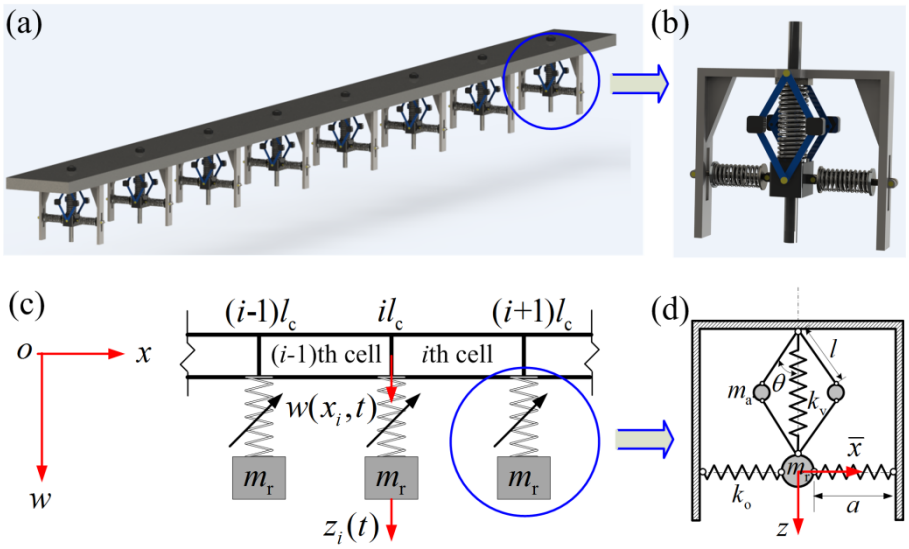

Fig. 1 Conceptual design schemes of (a) the LR-IAM beam with (b) HSLDS resonators containing IAM, and schematic diagrams of the computational models for (c) the LR-IAM beam and (d) the resonator.

2.1 Stiffness characteristics of the resonator

The HSLDS feature is realized by combining a vertical spring k_v and two oblique springs k_o in parallel, as shown in Figs. 1b and 1d. Assume that the mass of the resonator m_r can only move along the vertical direction, and two oblique springs deform symmetrically with respect to the vertical spring. At the static equilibrium position, these two oblique springs are compressed from the original length l_o to a, which act as a negative-stiffness mechanism in the vertical direction, when the resonator deviates from the static equilibrium. Additionally, a half of the IAM is constructed by using four light connecting rods and two masses, and the two halves of

the IAM are mirror symmetrical. These light rods have the same length l, which are symmetrically installed with respect to the vertical spring, and their weights are neglected. At the static equilibrium position, the intersection angle between the axis of the rod and the vertical spring is θ. These two masses also have the identical mass $m_a/2$, and the ratio of m_a to m_r is defined as

$$\gamma = \frac{m_a}{m_r} \tag{1}$$

Note that the IAM does not affect the static stiffness of the resonator. Therefore, the restoring force and stiffness of the HSLDS resonator as functions of the relative displacement $y = z - w$ can be given according to our previous work [29],

$$f = k_v \left[1 - (1-\eta) \frac{a}{l_o - a} \left(\frac{l_o}{\sqrt{a^2 + y^2}} - 1 \right) \right] y \tag{2}$$

$$k = k_v \left[1 - (1-\eta) \frac{a}{l_o - a} \left(\frac{l_o a^2}{\left[a^2 + y^2 \right]^{\frac{3}{2}}} - 1 \right) \right] \tag{3}$$

where z is the absolute displacement of the resonator, w is the transverse displacement of the beam, k_v is the stiffness of the vertical spring, l_o and a are the original and compressed lengths of the oblique spring, respectively, and η is a ratio of the designated stiffness of the resonator to k_v at the static equilibrium position. The above features of the restoring force and stiffness are achieved under the so-called *zero-stiffness* condition

$$\chi = \frac{k_o}{k_v} = \frac{(1-\eta)a}{2(l_o - a)} \tag{4}$$

where k_o is the stiffness of the oblique spring. Obviously, one can change the stiffness ratio χ or the geometrical parameters of the oblique springs to regulate the stiffness ηk_v of the HSLDS resonator, and even to tune it towards zero. In addition, from Eq. (3), it can be seen that the stiffness of the resonator is related to the displacement, and

it is equal to ηk_v only at the static equilibrium position. Therefore, the HSLDS resonator is nonlinear.

2.2 Inertial amplification mechanism

As shown in Fig. 1d, when the resonator oscillates around the static equilibrium point, the mass m_a moves both along the vertical and horizontal directions. There are two identical masses m_a in the IAM, and their vertical displacements are the same, but the horizontal displacements have opposite signs. The displacement components of the left mass from its original position are $\bar{x}_a$ and z_a, which can be described as functions of the displacement,

$$\bar{x}_a = l\sin\theta - \sqrt{l^2\sin^2\theta - yl\cos\theta - \frac{y^2}{4}}, \quad z_a = \frac{z+w}{2} \tag{5}$$

Recall that θ is the intersection angle between the axis of the rod and the vertical spring at the static equilibrium position, which is a constant (initial angle). Note that, when the oscillation is small, the original form of the displacement x_a in Eq. (5) can be linearized as $y\cot\theta/2$ by Taylor expansion at y=0, which is the same as that in Ref [23].

The velocity components of the left mass are

$$\dot{\bar{x}}_a = \frac{\left(2l\cos\theta + y\right)\dot{y}}{\sqrt{16l^2\sin^2\theta - 16yl\cos\theta - 4y^2}}, \quad \dot{z}_a = \frac{\dot{z}+\dot{w}}{2} \tag{6}$$

Therefore, the total kinetic energy T of the resonator can be given by

$$\begin{aligned} T &= \frac{1}{2}m_r\dot{z}^2 + 2\times\frac{1}{2}m_a\left(\dot{\bar{x}}_a^2 + \dot{z}_a^2\right) \\ &= \frac{1}{2}m_r\dot{z}^2 + \gamma m_r\dot{y}^2\frac{\left(2l\cos\theta + y\right)^2}{16l^2\sin^2\theta - 16yl\cos\theta - 4y^2} + \gamma m_r\frac{\left(\dot{z}+\dot{w}\right)^2}{4} \end{aligned} \tag{7}$$

where the dot above the displacement denotes differentiation with respect to time. In addition, taking the initial potential energy as a reference, the change in potential energy can be given by

$$U=\frac{1}{2}k_{\mathrm{v}}y^2+k_{\mathrm{o}}(y^2-2l_{\mathrm{o}}\sqrt{a^2+y^2}+2al_{\mathrm{o}}) \tag{8}$$

Furthermore, the equation of motion of the resonator can be obtained by using the Lagrange equation,

$$\begin{aligned}&\left(1+2\gamma\frac{l^2}{4l^2\sin^2\theta-4yl\cos\theta-y^2}\right)m_{\mathrm{r}}\ddot{y}+2\gamma m_{\mathrm{r}}\frac{l^2\left(2l\cos\theta+y\right)}{\left(4l^2\sin^2\theta-4yl\cos\theta-y^2\right)^2}\dot{y}^2\\&+k_{\mathrm{v}}\left[1-\left(1-\eta\right)\frac{a}{l_{\mathrm{o}}-a}\left(\frac{l_{\mathrm{o}}}{\sqrt{a^2+y^2}}-1\right)\right]y=-\left(1+\gamma\right)m_{\mathrm{r}}\ddot{w}\end{aligned} \tag{9}$$

Note that the second term of Eq. (9) represents an equivalent damping force, which is derived from the inertial effect of the IAM. Obviously, all of the effective mass, damping force and restoring force of the resonator are nonlinear functions with respect to the displacement. However, under small-amplitude vibrations, the nonlinear dynamic system could be simplified by employing linearization at the equilibrium point y=0,

$$\kappa m_r\ddot{y}+\eta k_{\mathrm{v}}y=-\left(1+\gamma\right)m_r\ddot{w} \tag{10}$$

where

$$\kappa=1+\frac{\gamma}{2\sin^2\theta} \tag{11}$$

is a magnification factor of the inertia. This linearized equation (10) has a similar form as the equation of motion of the inertial amplification mechanism in Ref [23]. Most importantly, the above linearized equation of motion will be utilized to calculate the dispersion relations of the LR-IAM beam by using transfer matrix method in the following Section 2.3.

Clearly, one can observe from Eq. (10) that the inertia of the resonator is amplified by the IAM, and the amplification is inversely proportional to $\sin^2\theta$, which implies that the smaller the incline angle θ is, the larger the inertia amplification one can achieve. Note that ηk_{v} is the net stiffness of the resonator at the static equilibrium

position after the neutralization by the negative-stiffness mechanism. Importantly, the parameter η can be tuned to be at any desired low value by adjusting the stiffness ratio α or the geometric parameters of the resonator.

2.3 Dispersion relations by using transfer matrix method

The equation of motion of an Euler-Bernoulli beam is

$$EI\frac{\partial^4 w}{\partial x^4}+\rho A\frac{\partial^2 w}{\partial t^2}=0 \tag{12}$$

where E is the module of elasticity, I is the moment of area, ρ is the density, A is the cross-sectional area, and $w(x, t)$ is the transverse deflection. By assuming the harmonic motion $w(x,t)=W(x)e^{\sqrt{-1}\omega t}$, where $W(x)$ is the mode function, as given by

$$W(x)=A\cos(\beta x)+B\sin(\beta x)+C\cosh(\beta x)+D\sinh(\beta x) \tag{13}$$

where A, B, C, and D are unknown constants, and $\beta^4=\omega^2\rho A/EI$. For the ith unit cell of the LR-IAM beam, the mode function can be written as

$$W_i(\tilde{x})=A_i\cos(\beta\tilde{x})+B_i\sin(\beta\tilde{x})+C_i\cosh(\beta\tilde{x})+D_i\sinh(\beta\tilde{x}) \tag{14}$$

where $\tilde{x}=x-il_{\mathrm{c}}$, $il_{\mathrm{c}}\le x\le(i+1)l_{\mathrm{c}}$, and l_{c} is the lattice constant, i.e. the length of the unit cell. The ith resonator is attached at $x=il_{\mathrm{c}}$, i.e. $\tilde{x}=0$, as shown in Fig. 1c. By assuming the harmonic small-amplitude oscillation of the ith resonator $y_i(t)=Y_ie^{\sqrt{-1}\omega t}$, the linearized equation of motion of the resonator (Eq. (10)) is used, and thus the force acting on the beam from the ith resonator can be given by

$$f_i(t)=\eta k_{\mathrm{v}}y_i(t)=\frac{\eta k_{\mathrm{v}}(1+\gamma)m_{\mathrm{r}}\omega^2}{\eta k_{\mathrm{v}}-\kappa m_{\mathrm{r}}\omega^2}W_i(0)e^{\sqrt{-1}\omega t} \tag{15}$$

Considering the continuities of the displacement, slope and bending moment at the connecting point of the resonator, as well as the change of shear force due to the connecting force $f_i(t)$, one can obtain the following boundary conditions

$$
\begin{aligned}
&W_{i-1}\left(l_{\mathrm{c}}\right)=W_i\left(0\right)\\
&W_{i-1}'\left(l_{\mathrm{c}}\right)=W_i'\left(0\right)\\
&W_{i-1}''\left(l_{\mathrm{c}}\right)=W_i''\left(0\right)\\
&W_{i-1}'''\left(l_{\mathrm{c}}\right)=W_i'''\left(0\right)-\frac{\eta k_{\mathrm{v}}\left(1+\gamma\right)m_{\mathrm{r}}\omega^2}{\eta k_{\mathrm{v}}-\kappa m_{\mathrm{r}}\omega^2}W_i\left(0\right)
\end{aligned}
\tag{16}
$$

By substituting Eq. (16) into Eq. (14), one can obtain the relations between the constants of the *i*th unit cell $\boldsymbol{\psi}_i=\left[A_i,\ B_i, C_i, D_i\right]^{\mathrm{T}}$ and the (*i*-1)th one, $\boldsymbol{\psi}_{i-1}$. Further, by employing the Floquet-Bloch theorem, $\boldsymbol{\psi}_i=e^{\sqrt{-1}ql_{\mathrm{c}}}\boldsymbol{\psi}_{i-1}$, one can derive the dispersion relation of the LR-IAM beam

$$
\left|\mathbf{G}^{-1}\mathbf{H}-e^{\sqrt{-1}ql_{\mathrm{c}}}\mathbf{I}\right|=0 \tag{17}
$$

where q is the wave number and $\mathbf{I}$ is the identity matrix, and

$$
\mathbf{H}=\begin{bmatrix}
\cos\left(\beta l_{\mathrm{c}}\right) & \sin\left(\beta l_{\mathrm{c}}\right) & \cosh\left(\beta l_{\mathrm{c}}\right) & \sinh\left(\beta l_{\mathrm{c}}\right)\\
-\beta\sin\left(\beta l_{\mathrm{c}}\right) & \beta\cos\left(\beta l_{\mathrm{c}}\right) & \beta\sinh\left(\beta l_{\mathrm{c}}\right) & \beta\cosh\left(\beta l_{\mathrm{c}}\right)\\
-\beta^2\cos\left(\beta l_{\mathrm{c}}\right) & -\beta^2\sin\left(\beta l_{\mathrm{c}}\right) & \beta^2\cosh\left(\beta l_{\mathrm{c}}\right) & \beta^2\sinh\left(\beta l_{\mathrm{c}}\right)\\
\beta^3\sin\left(\beta l_{\mathrm{c}}\right) & -\beta^3\cos\left(\beta l_{\mathrm{c}}\right) & \beta^3\sinh\left(\beta l_{\mathrm{c}}\right) & \beta^3\cosh\left(\beta l_{\mathrm{c}}\right)
\end{bmatrix} \tag{18}
$$

$$
\mathbf{G}=\begin{bmatrix}
1 & 0 & 1 & 0\\
0 & \beta & 0 & \beta\\
-\beta^2 & 0 & \beta^2 & 0\\
-\dfrac{1}{EI}\dfrac{\eta k_{\mathrm{v}}m_{\mathrm{r}}\omega^2}{\eta k_{\mathrm{v}}-\kappa m_{\mathrm{r}}\omega^2} & -\beta^3 & -\dfrac{1}{EI}\dfrac{\eta k_{\mathrm{v}}m_{\mathrm{r}}\omega^2}{\eta k_{\mathrm{v}}-\kappa m_{\mathrm{r}}\omega^2} & \beta^3
\end{bmatrix} \tag{19}
$$

The band structure of the LR-IAM beam can be obtained by solving the above dispersion relation. For any frequency ω, one can get four solutions for the wave number *q*. Note that the evanescent waves are not investigated here, and thus the two pure imaginary solutions are not considered. Moreover, when the solution is real, the flexural wave can propagate through the beam without attenuation. In contrast, the wave would be attenuated when the solution is imaginary in certain frequency ranges, called band gaps.

2.4 Band gaps

For the local resonant band gap, the lower bound frequency ω_{l} is determined by the natural frequency of the resonator, and the upper bound frequency ω_{u} is related to both the natural frequency of the resonator and the mass ratio of the resonator to the unit cell of the beam [8, 29], which can be given by

$$\omega_{\mathrm{l}}=\sqrt{\frac{\eta k_{\mathrm{v}}}{\kappa m_{\mathrm{r}}}},\quad \omega_{\mathrm{u}}=\sqrt{\frac{\eta k_{\mathrm{v}}}{\kappa m_{\mathrm{r}}}\left[1+\mu\left(1+\gamma\right)\right]} \tag{20}$$

where $\mu=m_{\mathrm{r}}/\rho A l_{\mathrm{c}}$. Recall that $\kappa=1+\gamma/\left(2\sin^{2}\theta\right)$ is the inertia magnification factor. When the resonator does not have the IAM and negative-stiffness mechanism, both κ and η are 1. Obviously, the bound frequencies can be tuned towards quite low values, when the negative-stiffness mechanism is active, causing η to become smaller than 1. In addition, when the IAM is switched on, κ become larger than 1, and thus, the bound frequencies also can be reduced by the IAM.

In order to highlight the effect of the IAM on the band gaps, the parameters are selected from our previous work [29], which did not consider any IAMs. For the sake of completeness, those parameters are listed in Table 1. From Eq. (11), one can see that the mass ratio γ and the incline angle θ of the connecting rod in the IAM are essential to inertial magnification. Therefore, the effects of these two parameters on the band gaps will be discussed in detail.

Table 1 Parameters of the LR-IAM beam

Parameters	Values
Module of elasticity E	70 GPa
Area moment of inertia I	5.968×10^{-9} m^4
Density ρ	2600 kg/m^3
Cross-sectional area A	1.602×10^{-4} m^2
Length of unit cell l_c	0.125 m
Mass of resonator m_r	0.0437 kg
Stiffness of vertical spring k_v	1.65×10^5 N/m
Length of oblique spring l_o	0.0459 m
Length of vertical spring l_v	0.05 m

The dispersion curves of the LR-IAM beam for different parameters are shown in Fig. 2, where the band gaps are illustrated by green shadow areas. In such frequency regions, the solutions of the wave number q are imaginary, which implies that the flexural wave in the LR-IAM beam would be attenuated.

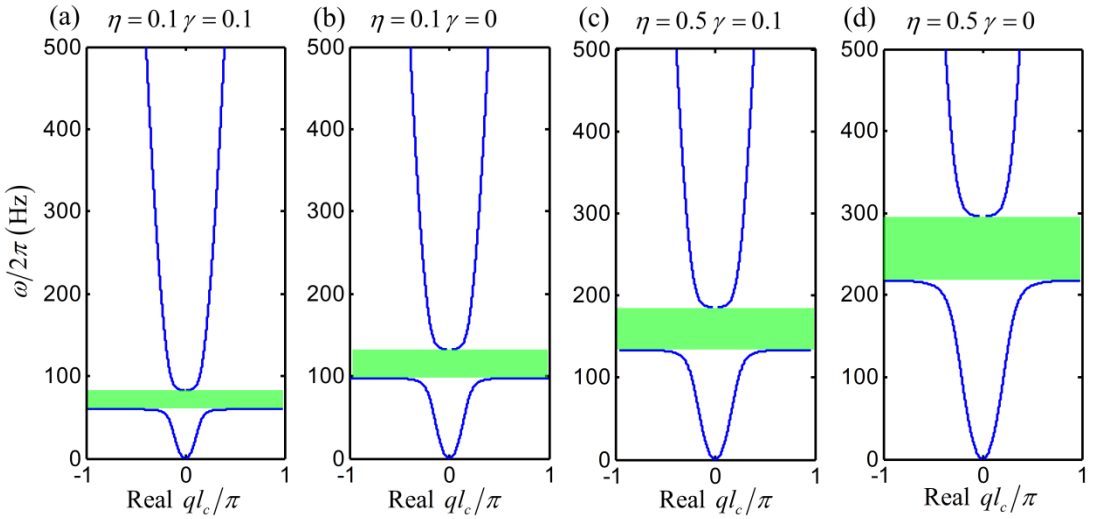

Fig. 2 Dispersion curves of the LR-IAM beam and the band gaps illustrated by the green shadow areas.

Furthermore, the lower and upper bound frequencies of the band gaps are illustrated with respect to the net stiffness of the resonator, as depicted in Fig.3. The band gaps are denoted by the green shadow areas surrounded by the bound frequencies, which are obtained by Eq. (20) and depicted as hollow marks. Obviously, the markers almost

coincide with the borders of the shadow areas, which means that the band gaps estimated by the analytical expressions match well the transfer matrix results.

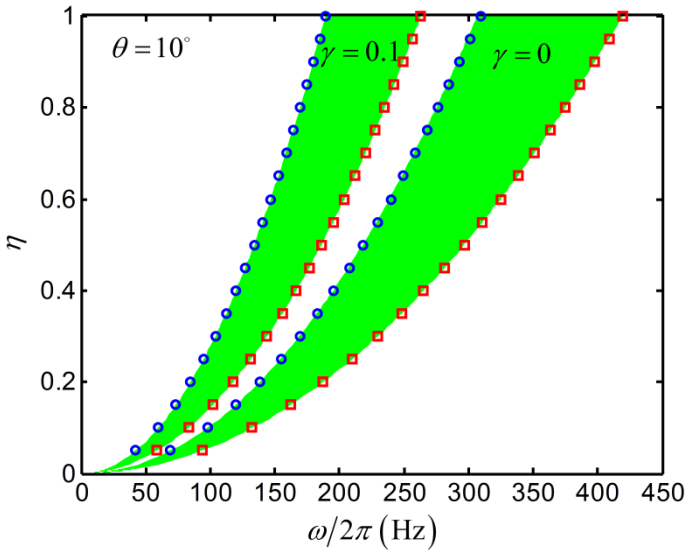

Fig. 3 Band gaps of the LR-IAM beam predicted by the transfer matrix method (green areas), and the lower and upper bound frequencies given by Eq. (20) and denoted by hollow markers, when the IAM is switched on ($\gamma = 0.1$) or off ($\gamma = 0$).

As expected, the bound frequencies decrease as the net stiffness ratio η is tuned from 1 to 0. This is an interesting and inherent feature of the metamaterials with HSLDS local resonators, whose net stiffness can be tuned towards any designated low values by adjusting the negative-stiffness element to partly or totally neutralize the stiffness of the positive-stiffness element.

More importantly, from Fig. 2 and Fig. 3, one can observe that both the lower and upper bound frequencies of the band gaps are substantially shifted towards lower frequencies by the IAM, even with a small mass ratio $\gamma = 0.1$, i.e. 20% of the resonator mass ($2m_a/m_r$), and 8.36% of the unit cell mass ($2m_a/(m_r + 2m_a + \rho A l_c)$). Additionally, the lower and upper bound frequencies are reduced by the proportion of $1-1/\sqrt{\kappa}$ and $1-\vartheta/\sqrt{\kappa}$ ($\vartheta = \sqrt{[1+\mu(1+\gamma)]/(1+\mu)}$), respectively, for a selected θ. For example, in Fig. 3, the lower and upper bound frequencies are reduced by 38.7%

and 37.3%, respectively, for all the values of η, when $\theta = 10^{\circ}$.

The effects of the parameters of the IAM on the bound frequencies ω_{l} and ω_{u} of the band gaps are shown in Fig. 4. As seen from Fig. 4a, the bound frequencies are reduced by increasing the mass of the IAM, which can be attributed to the fact that the inertial amplification factor κ is in proportion to the mass ratio γ, and the bound frequencies vary inversely with $\sqrt{\kappa}$. However, the influence of γ on the bound frequencies decreases step by step with increasing γ. As mentioned before, even a small γ could lead to large reductions in the bound frequencies. Therefore, for the proposed IAM, a large physical mass is not indispensable to magnify the inertia of the resonator, and a small one could perform well, which agrees well with the finding by Yilmaz et al. [20].

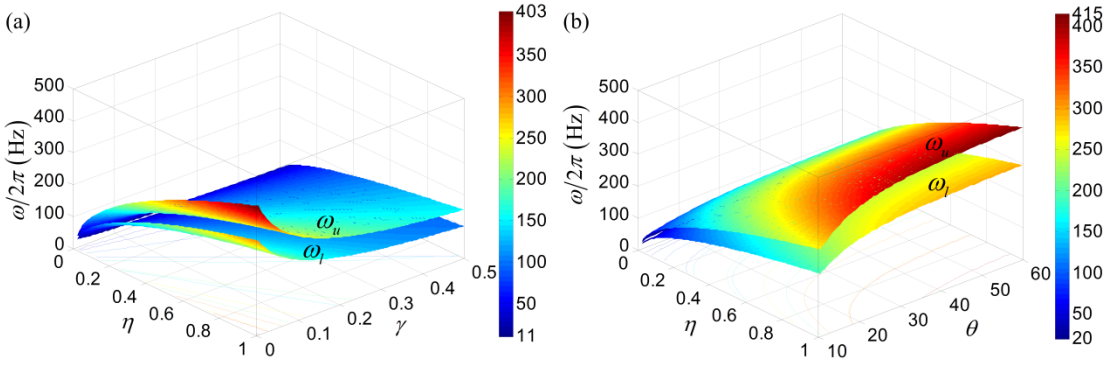

Fig. 4 Effects of the parameters of the IAM on the bound frequencies ω_l and ω_u of the band gaps. (a) Mass ratio γ when $\theta = 10^{\circ}$; (b) incline angle θ when $\gamma = 0.1$.

The effect of the incline angle θ is shown in Fig. 4b. Obviously, the bound frequencies are increased but the increases are reduced as θ increases. From Eq. (11), one also can find that the smaller the incline angle θ is, the larger the inertial amplification is. This trend also has good agreement with that observed by Yilmaz et al. [20]. Hence a small incline angle θ is preferable theoretically. Nevertheless, the mobility of the resonator should be taken into account. A small incline angle θ

would limit the mass of the resonator to move free along the vertical direction in a very small displacement range, which would be detrimental to the locally resonant mechanism. Therefore, the incline angle θ should be as small as possible, under the pre-condition for the mobility of the resonator.

3. Wave attenuations in the LR-IAM beams

The dynamic responses of the LR-IAM beams with finite length are obtained by employing Galerkin discretization, and then the wave attenuations are evaluated in terms of displacement transmittance. Firstly, the first three modes of the beam are taken into account to reveal the amplitude-frequency characteristics of the LR-IAM beam analytically. Then, fifteen modes are considered, and the equations of motion are solved numerically to calculate the transmittance. Finally, the global bifurcation and nonlinear dynamic behaviours of the LR-IAM beam are studied.

The equations of motion of the finite-length LR-IAM beam can be given by

$$EI\frac{\partial^4 w}{\partial x^4}+\rho A\frac{\partial^2 w}{\partial t^2}=f_{\mathrm{e}}(t)\delta(x-0)+\sum_{i=1}^{n}\left[f_{\mathrm{d}}(x_i,t)+f_{\mathrm{s}}(x_i,t)\right]\delta(x-x_i) \tag{21}$$

$$m_{\mathrm{e}}\ddot{y}(x_i,t)+f_{\mathrm{d}}(x_i,t)+f_{\mathrm{s}}(x_i,t)=-(1+\gamma)m_{\mathrm{r}}\ddot{w}(x_i,t),\quad i=1,\,2,\cdots n \tag{22}$$

where n is the number of resonators, $\delta(x)$ is the Dirac function, $f_{\mathrm{e}}(t)$ is the excitation force acting on the left-hand end of the beam (x=0), $f_{\mathrm{d}}(x_i,t)$ and $f_{\mathrm{s}}(x_i,t)$ are the internal damping and restoring forces between the resonator and beam (x=x_i), respectively, and m_{e} is the effective mass of the resonator with the IAM. According to Eq. (9), m_{e}, f_{d} and f_{s} can be given by

$$m_{\mathrm{e}}=\left(1+2\gamma\frac{l^2}{4l^2\sin^2\theta-4y_i l\cos\theta-y_i^{\,2}}\right)m_{\mathrm{r}} \tag{23}$$

$$f_{\mathrm{d}} = 2\gamma m_{\mathrm{r}} \frac{l^2\left(2l\cos\theta + y_i\right)}{\left(4l^2\sin^2\theta - 4y_i l\cos\theta - y_i^{\,2}\right)^2}\dot{y}_i^{\,2} \tag{24}$$

$$f_{\mathrm{s}} = k_{\mathrm{v}}\left[1-(1-\eta)\frac{a}{l_{\mathrm{o}}-a}\left(\frac{l_{\mathrm{o}}}{\sqrt{a^2+y_i^{\,2}}}-1\right)\right]y_i \tag{25}$$

Note that $y_i(t) = z_i(t) - w(x_i,t)$ is the relative displacement of the *i*th resonator. Obviously, all of the effective mass, the restoring force and the damping force are nonlinear functions of the relative displacement.

According to Galerkin discretization, the response of the beam can be assumed as

$$w(x,t) = \sum_{p=1}^{P} W_p(x)Q_p(t) \tag{26}$$

where $W_p(x)$ and $Q_p(t)$ are the mode function and generalized displacement, respectively. For the free-free end condition, the mode function $W_p(x)$ of the beam can be given by

$$\begin{aligned} W_p(x) &= \sin(\beta_p x) + \sinh(\beta_p x) \\ &\quad + \frac{\sin(\beta_p L) - \sinh(\beta_p L)}{\cosh(\beta_p L) - \cos(\beta_p L)}\left[\cos(\beta_p x) + \cosh(\beta_p x)\right] \quad p = 1, 2\cdots \end{aligned} \tag{27}$$

where L is the length of the beam, and

$$\beta_p^4 = \frac{\rho A\omega_p^2}{EI} \tag{28}$$

where ω_p is the *p*th natural frequency of the beam, which is determined by the frequency equation, $\cos\beta_p L\cosh\beta_p L = 1$.

By substituting Eq. (26) into Eq. (21), multiplying both sides of the resultant equation by the mode function $W_p(x)$, and then integrating along the length of the beam L, one can obtain

$$m_p\ddot{Q}_p + k_p Q_p = W_p(0)\, f_{\mathrm{e}}(t) + \sum_{i=1}^{n} W_p(x_i)\left[f_{\mathrm{d}}(x_i,t) + f_{\mathrm{s}}(x_i,t)\right] \tag{29}$$

where $m_p = \rho A\int_0^L W_p^2(x)\mathrm{d}x$, and $k_p = EI\int_0^L W_p^{(4)}(x)W_p(x)\mathrm{d}x$. Note that the superscript (4) denotes the 4th partial derivative with respect to *x*.

3.1 Approximately analytical solutions

In order to analytically reveal the dynamic response of the LR-IAM beam when the nonlinearity is taken into account, all the expressions of effective mass m_{e}, restoring force f_{s} and damping force f_{d} are approximated by Taylor expansions at the static equilibrium position $y_i = 0$, as listed below

$$\tilde{m}_{\mathrm{e}} = \mathrm{M}_0 + \mathrm{M}_1 y_i + \mathrm{M}_2 y_i^2 = \kappa m_{\mathrm{r}} + \frac{\gamma\cos\theta m_{\mathrm{r}}}{2l\sin^4\theta} y_i + \frac{\gamma\left(1+3\cos^2\theta\right)m_{\mathrm{r}}}{4l^2\sin^6\theta} y_i^2 \tag{30}$$

$$\begin{aligned}\tilde{f}_{\mathrm{d}} &= \left(\Gamma_{\mathrm{d}0} + \Gamma_{\mathrm{d}1} y_i + \Gamma_{\mathrm{d}2} y_i^2\right)\dot{y}_i^2 \\ &= \left[\frac{m_{\mathrm{r}}\gamma\cos\theta}{4l\sin^4\theta} + \frac{m_{\mathrm{r}}\gamma\left(1+3\cos^2\theta\right)}{8l^2\sin^6\theta} y_i + \frac{3m_{\mathrm{r}}\gamma\cos\theta\left(1+\cos^2\theta\right)}{4l^3\sin^8\theta} y_i^2\right]\dot{y}_i^2\end{aligned} \tag{31}$$

$$\tilde{f}_{\mathrm{s}} = \Gamma_{\mathrm{s}1} y_i + \Gamma_{\mathrm{s}3} y_i^3 = k_{\mathrm{v}}\eta y_i + k_{\mathrm{v}}\frac{(1-\eta)l_{\mathrm{o}}}{(l_{\mathrm{o}}-a)a^2} y_i^3 \tag{32}$$

Both the exact expressions and the approximate ones of the effective mass, damping coefficient and restoring force are depicted in Fig. 5. Obviously, in most of the displacement range, the approximations are in good agreement with the exact ones, especially in the vicinity of the equilibrium point y_i=0. Therefore, these approximate expressions of the effective mass, damping force and restoring force in Eqs. (30)-(32) can be used for the following dynamic study for approximately analytical solutions of the LR-IAM beam. It also can be observed that the effective mass and damping coefficient might approach infinity when the relative displacement y_i is close to its critical value $y_{\mathrm{cri}} = l(1-\cos\theta)$. This critical condition happens when the intersectional

angle of these two connecting rods becomes 180° and their axes are parallel with the vertical direction, which is an extreme position for the resonator. Additionally, the effective mass and damping coefficient become very large to prevent the resonator from getting across the limit position, as the displacement approaches the critical value.

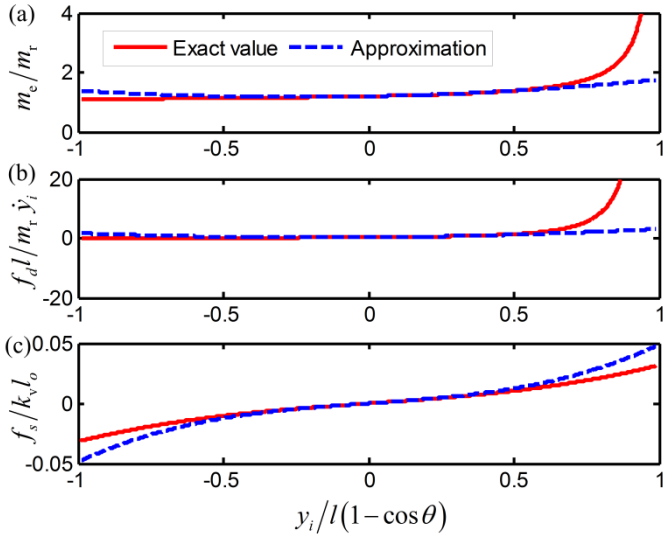

Fig. 5 Comparison between the exact values (solid lines) and the approximations (dashed lines) of (a) effective mass, (b) damping coefficient and (c) restoring force of the resonator, when $\eta = 0.1$, $\gamma = 0.1$ and $\theta = 30^\circ$.

The responses of the beam are mainly dominated by the low-order modes, and the central frequency of the band gap is much lower than the lowest natural frequency of the beam. In addition, the analytical solutions of a high-dimensional nonlinear system are hard to be achieved. Hence, only the first three modes of the beam and only two resonators at x_1=L/3 and x_2=2L/3 are considered here as an example to analytically reveal the band gaps and the effect of nonlinearity on the band gaps. Taking into account the mode damping of the beam, the equations of motion of the LR-IAM beam can be rewritten as

$$\begin{aligned} &m_p\ddot{Q}_p + 2\zeta_p\sqrt{m_p k_p}\dot{Q}_p + k_p Q_p \\ &= \sum_{i=1}^{2} W_p(x_i)\left[\left(\Gamma_{d0} + \Gamma_{d1} y_i + \Gamma_{d2} y_i^2\right)\dot{y}_i^2 + \left(\Gamma_{s1} y_i + \Gamma_{s3} y_i^3\right)\right] + W_p(0)\, f_e(t), \quad p = 1,2,3 \end{aligned} \tag{33}$$

$$\begin{aligned}&\left(\mathrm{M}_0+\mathrm{M}_1 y_i+\mathrm{M}_2 y_i^2\right)\ddot{y}_i+\left(\Gamma_{\mathrm{d}0}+\Gamma_{\mathrm{d}1} y_i+\Gamma_{\mathrm{d}2} y_i{}^2\right)\dot{y}_i{}^2+\left(\Gamma_{\mathrm{s}1} y_i+\Gamma_{\mathrm{s}3} y_i^3\right)\\&=-(1+\gamma) m_{\mathrm{r}} \sum_{p=1}^{3} W_p\left(x_i\right)\ddot{Q}_p, \qquad i=1,2\end{aligned} \tag{34}$$

where ζ_p is the mode damping ratio, and $f_{\mathrm{e}}(t)=F_0\cos\omega t$ is a harmonic external force acting at the left-hand end of the beam (x=0). Assume the fundamental solutions are harmonic

$$\begin{aligned}&Q_p=\Theta_{p0}+\Theta_{p1}\cos\omega t+\Theta_{p2}\sin\omega t, \quad p=1,2,3\\&y_i=Y_{i0}+Y_{i1}\cos\omega t+Y_{i2}\sin\omega t, \quad i=1,2\end{aligned} \tag{35}$$

By substituting Eq. (35) into Eq. (33) and Eq. (34) and equating the coefficient of each of the harmonics to zero, one can obtain 15 algebraic equations relating Θ_{p0}, Θ_{p1}, Θ_{p2} (p=1, 2, 3) and Y_{i0}, Y_{i1}, Y_{i2} (i=1, 2) can be obtained, as given in Appendix A.

The amplitude-frequency relations of the LR-IAM beam under a harmonic force are depicted in Fig. 6, when $F_0=10$ N, $\eta=0.1$, $\gamma=0.1$, $\theta=30^\circ$ and $\zeta_p=0.05$ $(p=1,\ 2,3)$. The vibration amplitudes at the left-hand end x=0 and at the right-hand end x=L can be given by

$$\begin{aligned}W(0)&=\sqrt{\left(\sum_{p=1}^{3} W_p(0)\Theta_{p1}\right)^2+\left(\sum_{p=1}^{3} W_p(0)\Theta_{p2}\right)^2}\\W(L)&=\sqrt{\left(\sum_{p=1}^{3} W_p(L)\Theta_{p1}\right)^2+\left(\sum_{p=1}^{3} W_p(L)\Theta_{p2}\right)^2}\end{aligned} \tag{36}$$

which are shown in Fig. 6a and Fig. 6b, respectively. To validate the approximate analytical solutions, numerical simulations are also carried out by numerically solving the equations of motion of the LR-IAM beam (Eq. (33) and Eq. (34)) with the Runge-Kutta algorithm. Both forward and backward sweep frequency response analyses are done to reveal the jump phenomenon and multi-solution characteristics of the nonlinear system.

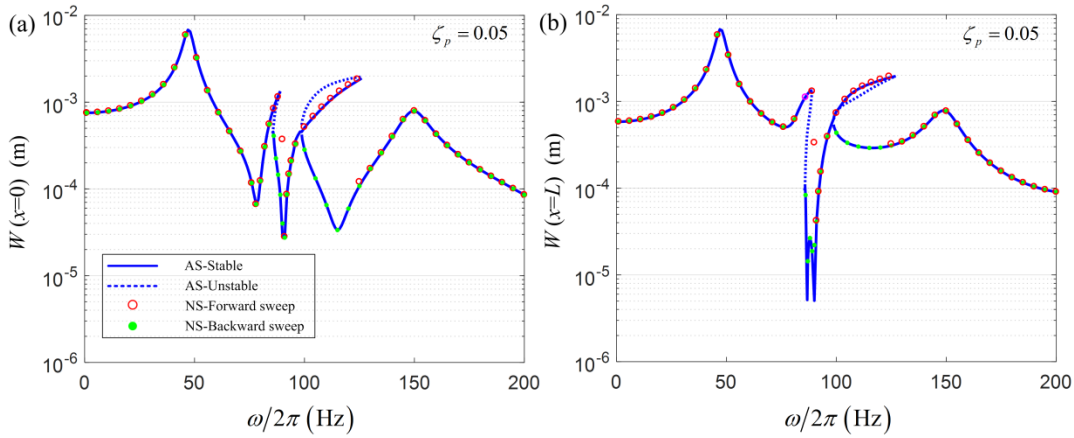

Fig. 6 Amplitude-frequency relations of the LR-IAM beam (a) at x=0 and (b) at x=L, when $F_0 = 10$ N, $\gamma = 0.1$, $\eta = 0.1$, $\theta = 30^\circ$ and $\zeta_p = 0.05$ $(p = 1,\ 2, 3)$. Solid and dashed lines represent stable analytical solution (AS-Stable) and unstable one (AS-Unstable), respectively. Hollow and solid circles denote the numerical simulations by forward sweep frequency response analysis (NS-Forward sweep) and backward one (NS-backward sweep), respectively.

In Fig.6, the analytical solutions are represented by lines, including stable one (solid line) and unstable one (dashed line), and the numerical solutions obtained by using sweep frequency response analysis are denoted by circular dots, including forward sweep (hollow circle) and backward sweep (solid circle). Obviously, there is excellent agreement between the analytical solutions and the numerical ones, which verifies the accuracy of the analytical solutions.

Furthermore, there are three branches for response amplitudes in two frequency bands from 85.5Hz Hz to 89Hz and from 98Hz to 124Hz, which is an inherent multi-solution feature of a nonlinear dynamic system. The numerical solutions by forward sweep (hollow circle) can predict the resonant amplitude and the jump-down phenomenon, while those by backward sweep (solid circle) is capable of revealing the non-resonant amplitude on the lowest branch and the jump-up phenomenon. Nevertheless, one of the three analytical solutions cannot be obtained by both the forward and backward sweep frequency analyses, which could be considered as an unstable and unrealized solution [39].

On the lowest branch, notable vibration attenuations can be observed in the vicinity of

the resonant frequency 89.28Hz. In addition, the vibration attenuation at the right-hand end (x=L) are much larger than that at the left-hand end (x=0), which implies flexural wave attenuations along the LR-IAM beam by the attached resonators, when the driving frequency falls into the band gap. However, when the response amplitude is on the resonant branch, no vibration attenuation can be observed around the resonant frequency 89.28 Hz.

As well-known, the resonant responses are sensitive to damping. Fig. 7 shows the analytical solutions when the mode damping ratio is selected as $\zeta_p = 0.005\ (p = 1,\ 2, 3)$. Comparing Fig. 7 and Fig. 6, it can be observed that, with decrease in the damping ratio, the resonant branch becomes longer, which implies that the frequency band of multiple solutions is broadened, and the possibility of undergoing large-amplitude responses is increased. From the perspective of vibration or wave attenuations, relative large damping is needed for the LR-IAM beam to effectively narrow the multi-solution frequency band and suppress the jump phenomenon.

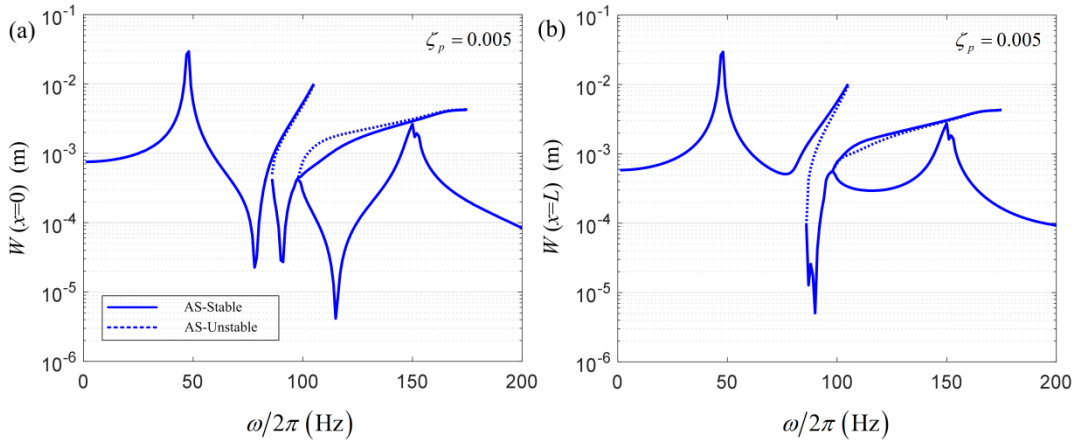

Fig. 7 Amplitude-frequency relations of the LR-IAM beam (a) at x=0 and (b) at x=L, when $F_0 = 10$ N, $\gamma = 0.1$, $\eta = 0.1$, $\theta = 30^\circ$ and $\zeta_p = 0.005\ (p = 1,\ 2, 3)$. Solid and dashed lines represent stable analytical solution (AS-Stable) and unstable one (AS-Unstable), respectively.

Moreover, which branch the response would locate on is determined by the initial condition of the LR-IAM beam. The influence of the initial condition of the resonator

on the response of the LR-IAM beam is demonstrated in Fig. 8, where x_0 and $\dot{x}_0$ are the initial displacement and velocity of the resonator at x_1=L/3, respectively. Both the beam and the resonator at x_2=2L/3 are in rest state at the beginning. Thus, the initial condition for numerically solving Eq. (33) and Eq. (34) is (0, 0, 0, 0, 0, 0, x_0, $\dot{x}_0$, 0, 0). In Fig. 8, the initial condition making the LR-IAM beam undergo resonant response is marked as cross, while that leading to non-resonant response is denoted as hollow circle. Note that the excitation frequency $\omega = 178\pi$ is selected from the band gap.

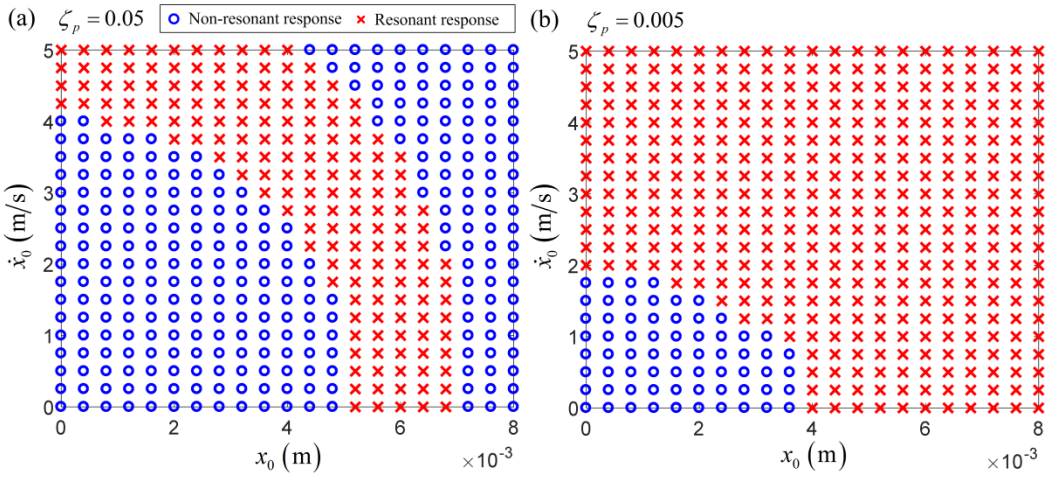

Fig. 8 Response dependence of the LR-IAM beam on the initial condition. (a) $\zeta_p = 0.05$, (b) $\zeta_p = 0.005$ $(p = 1,\ 2, 3)$, when $F_0 = 10$ N, $\gamma = 0.1$, $\eta = 0.1$, $\theta = 30^\circ$ and $\omega = 178\pi$. Hollow circles and crosses represent the non-resonant and resonant responses, respectively

Apparently, there exists a region of initial condition for resonant response, which would make the response fall onto the resonant branch. In such a case, neither the vibration mitigations of the host beam nor the attenuations of flexural wave propagating along the LR-IAM beam occur. Additionally, comparing Fig. 8b with Fig. 8a, one can see that the initial-condition region of resonant response becomes larger as the damping is reduced. Nonetheless, when the damping is relative heavy and the initial displacement and velocity are small, as shown in the down-right area of Fig. 8a, the response will fall onto the non-resonant branch, and the vibration and wave attenuation can be achieved.

Practically, the LR-IAM beam is in a state of rest at the beginning (*zero* initial condition), and both the beam and the resonators have physical damping. As a result, the response corresponds to the lowest non-resonant branch in most cases. Therefore, the LR-IAM beam is effective for low-frequency flexural wave attenuations, as long as the LR-IAM beam is not in an initial state to make the response approach the resonant branch.

3.2 Numerical simulations

In this section, the dynamic system of the LR-IAM beam is solved by a numerical method. The attenuation performance of the flexural wave propagating along the LR-IAM beam is evaluated in terms of the transmittance, which is defined as the ratio of the transverse vibration amplitude at the free end of the beam (x=L) to that at the end where an excitation force is acting (x=0). All of the exact expressions for the nonlinear effective mass (Eq. (23)), damping force (Eq. (24)) and storing force (Eq. (25)) are taken into account here to obtain the responses of the LR-IAM beam. In addition, the responses are calculated by numerically solving both the equations of motion of the beam in generalized coordinates (Eq. (29)) and those of the resonators (Eq. (22)) using Runge-Kutta method. Note that fifteen modes ($P=15$) of the beam are considered in the Garlerkin discretization, and the modal damping factor 0.1 for each mode is taken into account to make the transient responses die away quickly.

For different net stiffness of the resonator, the transmittances are depicted in the form of 3D plots and contour plots, respectively, in Fig. 9, when 24 resonators are attached onto the beam and $\gamma=0.1,\ \eta=0.1,\ \theta=10^{\circ}$. Obviously, there is a green gap where the transmittance in dB is below zero, which implies wave attenuations when the frequency of the flexural wave locates in such a band gap. By Comparing Fig. 9b with Fig. 3, one can see good agreement between the theoretical prediction of the band gap and that revealed by numerical simulations, when the IAM is switched on ($\gamma=0.1$).

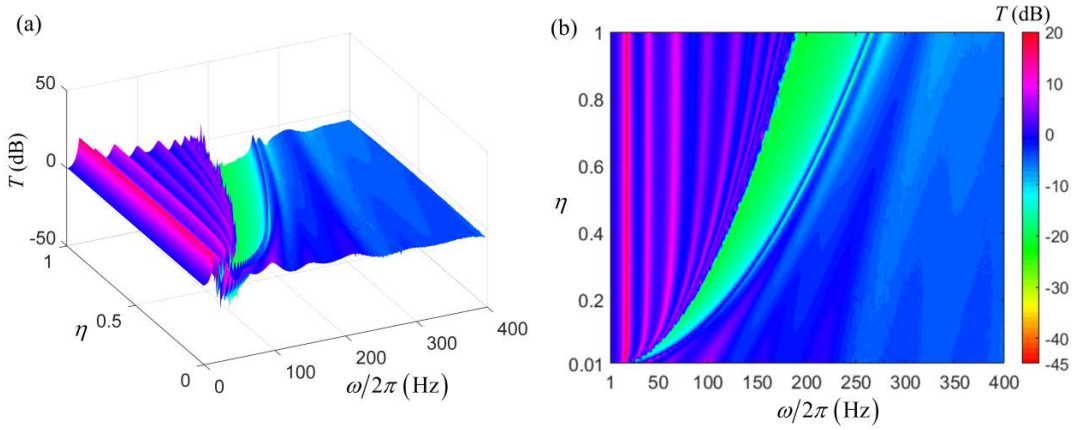

Fig. 9 Transmittance of the flexural wave propagating along the LR-IAM beam for different net stiffness of the resonator when *n*=24, $\gamma = 0.1$, $\eta = 0.1$ and $\theta = 10^{\circ}$. (a) 3D plot and (b) contour plot. The green area demonstrates the band gap for wave attenuations.

From Fig. 9, one also can see that the band gap moves towards a lower frequency and becomes narrower as the net stiffness of the resonator decreases, because both the lower and upper frequencies can be reduced by decreasing the net stiffness, as mentioned in Section 2.4. Therefore, the band gap for wave attenuations in this LR-IAM beam can be effectively tuned towards a desired low frequency by adjusting the net stiffness of the resonator with the IAM.

3.2.1 Effects of the parameters of the IAM on wave attenuation

The effects of the parameters γ and θ of the IAM on wave attenuation are demonstrated in Fig. 10, where the conspicuous green areas with the minus transmittances represent the band gaps. It can be seen from Fig. 10 that the bound frequencies of the band gap are reduced as the ratio γ of the mass of the IAM to that of the resonator increases, while the band gap moves towards higher frequency range and become wider as the incline angle θ of the connecting rod in the IAM increases. Additionally, these observations match well with theoretical predictions presented in Fig. 4. Most importantly, one can also observe that the LR-IAM beam can effectively attenuate the flexural wave, even when the band gap locates in a very low-frequency range by tuning the net stiffness of the resonator towards a very low value, such as η=0.1, and by adding the IAM with small incline angle and large mass ratio, such as

θ=10° and γ=0.5.

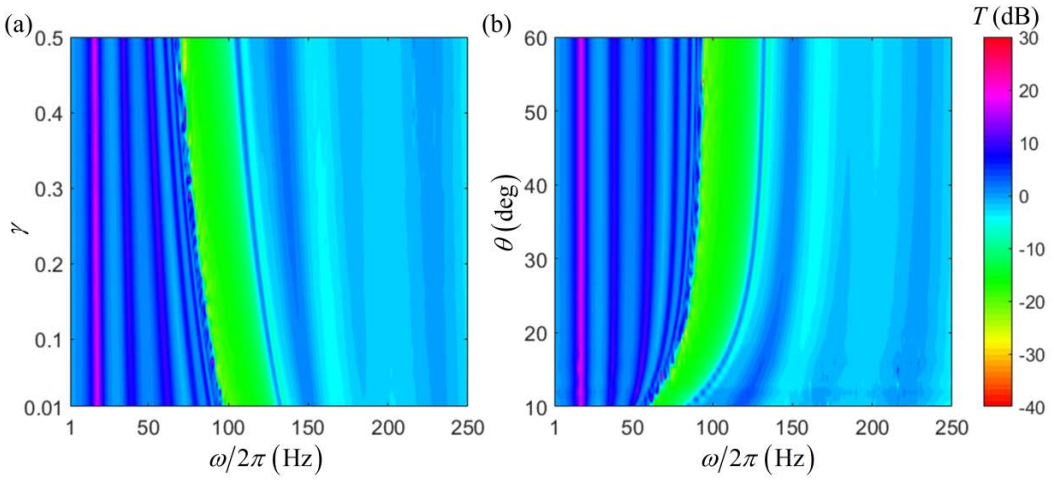

Fig. 10 Effects of the parameters of IAM on the transmittances. (a) Mass ratio γ with $\eta = 0.1$ and $\theta = 30^\circ$, (b) incline angle θ with $\eta = 0.1$ and $\gamma = 0.1$.

3.2.2 Effects of nonlinearity on wave attenuation

In general, the nonlinearity is related to the displacement amplitude, which cannot be ignored as the excitation amplitude increases. The strong nonlinearity might cause complicated dynamic behaviours, such as quasi-periodic and chaotic oscillations. Both the bifurcation diagram (maximum amplitude) of the transverse displacement responses at x=0 and x=L are plotted as functions of the excitation amplitude F_0 in Fig. 11, when $\gamma = 0.1$, $\eta = 0.1$ and $\theta = 30^\circ$. Note that the harmonic excitation acts at x=0, and the driving frequency 95Hz locates in the band gap.

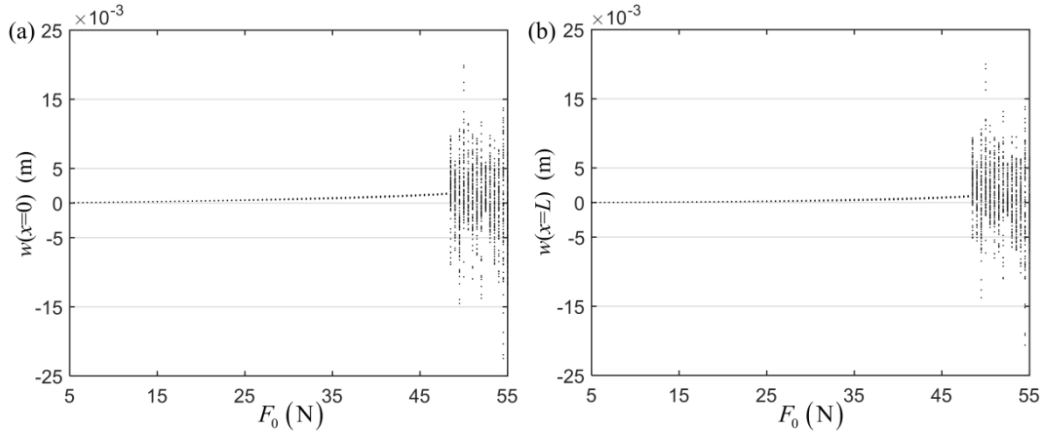

Fig. 11 Bifurcation diagram of the responses of the LR-IAM beam with respect to the excitation amplitude when $\omega = 190\pi$ rad/s, $\theta = 30^\circ$, $\gamma = 0.1$ and $\eta = 0.1$. (a) Displacement response at x=0; (b) displacement at x=L.

From Fig. 11, one can see a route to chaos [40], which shows how the response of the transverse displacement of the LR-IAM beam changes from periodic motion to chaotic one, when the excitation amplitude increases from 5N to 55N. Obviously, at F_0=48.35N, the response suddenly changes into chaotic motion. In order to reveal the dynamic behaviour, the phase portraits and the corresponding Poincare sections under zero initial condition and an excitation with different amplitudes are illustrated in Fig. 12. The scales of both the abscissa and ordinate are fixed to be identical for the same excitation amplitude, and thus one can clearly observe the flexural wave attenuation along the LR-IAM beam by comparing the response at x=L to that at x=0.

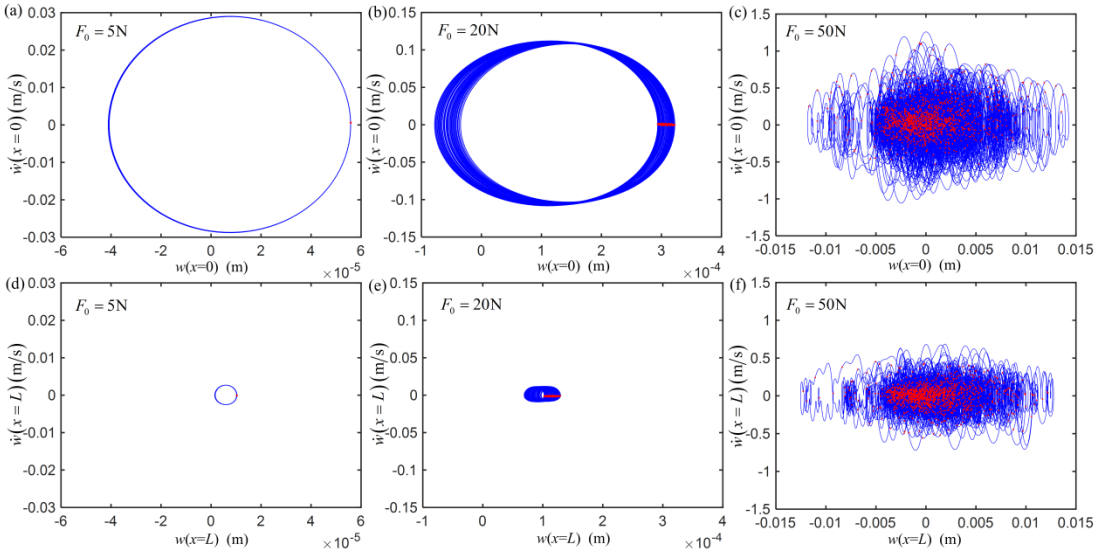

Fig. 12 Phase portraits (blue curves) and the corresponding Poincare sections (red markers). The upper and lower rows are for the responses at x=0 and x=L, respectively. (a) (d) F_0=5N; (b) (e) F_0=20N, (c) (f) F_0=50N, when $\omega = 190\pi$ rad/s, $\theta = 30^\circ$, $\gamma = 0.1$ and $\eta = 0.1$.

It can be seen from Fig. 12a and Fig. 12d that, for the responses at both ends, the phase portrait is a circle and the Poincare section is a point, so that the responses are periodic when F_0=5N. However, as the exciting amplitude F_0 increases, the dynamic behaviours might become more complicated. For example, when F_0=20N, the phase portrait contains many elliptic orbits, and the Poincare section is a very flat and closed curve, which seems like a line, as shown in Fig. 12b and Fig. 12e; therefore, the responses are quasi-periodic. When the excitation is increased further, such as

F_0=50N, the phase portrait becomes cluttered with orbits, and the Poincare section is composed of a cloud of points, as presented in Fig. 12c and Fig. 12f, which implies that the responses might be chaotic for a light damped nonlinear system.

More importantly, by comparing Fig. 12a and Fig. 12d, Fig. 12b and Fig. 12e, respectively, one can observe that the response at $x=L$ is much smaller than that at x=0, which means that flexural wave attenuations occur in the band gap when the responses are periodic or quasi-periodic. But, by comparing Fig. 12c and Fig. 12f, it can be seen that the maximum transverse displacement response at $x=L$ is close to that at x=0, which indicates that the attenuation of displacement cannot be realized when the responses are chaotic, although the mitigation of transverse velocity can be observed. This is an interesting feature for manipulating flexural wave. This proposed LR-IAM beam can be used as an amplitude-dependent filter to attenuate the small-amplitude wave while pass the large-amplitude wave.

3.2.3 Effects of periodicity on wave attenuation

Generally, the spatial arrangement of the resonator plays no significant role in determining the main characteristics of a LR beam [10, 41]. To study the effect of losing periodicity on wave attenuation, five resonators are removed randomly from the original periodic LR-IAM beam with 24 resonators for two cases, and the numbers of the removed resonators are (2, 3, 5, 10, 21) and (1, 10, 12, 19, 23), respectively. The wave transmittances for such two cases are demonstrated in Fig. 13a and Fig. 13b, respectively, when $\gamma = 0.1,\ \eta = 0.1,\ \theta = 10^{\circ}$.

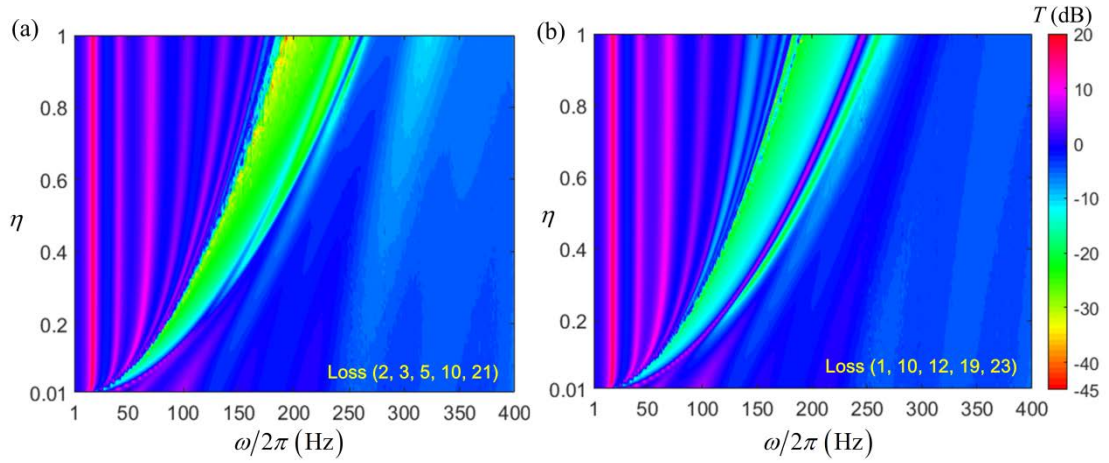

Fig. 13 Effects of periodicity on the transmittances. The numbers of the removed resonators are (a) (2, 3, 5, 10, 21) and (b) (1, 10, 12, 19, 23), when *n*=24, $\eta = 0.1$, $\theta = 10^{\circ}$ and $\gamma = 0.1$.

Comparing Fig. 13 with Fig. 9b, one can observe that losing periodicity has no impact on the lower bound frequency (i.e. central frequency) of the band gap. This is because the central frequency is only related to the resonant frequency but independent of the periodicity of the locally resonant structure [10]. However, the bandwidth and wave attenuation of the LR-IAM beam can be influenced by losing periodicity, which can be attributed to a fact that removing resonators at different locations results in different natural frequencies and mode shapes of the LR-IAM beam, especially for high order ones. For example, it can be seen from Fig. 13 that there is good agreement of the first five resonance peaks between these two cases, but differences would appear for higher order resonant peaks.

4. Conclusions

In this paper, a high-static-low-dynamic-stiffness (HSLDS) resonator with an inertial amplification mechanism (IAM) is developed as an elastic metamaterial structure that can attenuate very low-frequency flexural wave propagation along an Euler-Bernoulli beam. The static and dynamic features of the IAM are studied to reveal how this mechanism magnifies the inertia of the resonator. The band gaps are determined by both theoretical predictions (transfer matrix method) and numerical simulations

(Galerkin discretization). The results indicate that the proposed beam with inertially amplified resonators exhibits a capability of creating a very low-frequency band gap, when the net stiffness of the resonator is tuned to an ultra-low value. Moreover, a relatively large mass ratio and a small incline angle of the IAM are favourable to achieve better wave attenuations.

Furthermore, the nonlinearity, caused by the restoring force of the HSLDS resonator as well as both the damping force and effective inertia of the IAM, is studied analytically and numerically. This indicates that the nonlinearity leads to strong amplitude-dependent wave attenuation, which could be used as an amplitude-dependent switch or filter to control flexural waves. Additionally, damping has a significant impact on the multi-value feature of the LR-IAM beam. Light damping can increase the frequency range of multiple solutions and cause resonance more easily, which would reduce the wave attenuation capability. The periodicity on the wave transmittance is also discussed, which shows that losing periodicity has no effect on the central frequency of the band gap, but has influences on the bandwidth and wave attenuation.

Acknowledgements

This research work was supported by National Key R&D Program of China (2017YFB1102801), National Natural Science Foundation of China (11572116), and Natural Science Foundation of Hunan Province (2016JJ3036).

Declarations of interest

The authors declare no conflict of interest.

References

1. Lou J., Zhu S., He L., Yu X.: Application of chaos method to line spectra reduction. J. Sound Vib. **286**(3), 645-652 (2005)
2. Rivin E.I.: Passive Vibration Isolation. American Society of Mechanical Engineers Press, New York (2003)
3. Wang X., Zhou J. X., Xu D. L., Ouyang H. J., Duan Y.: Force transmissibility of a two-stage vibration isolation system with quasi-zero stiffness. Nonlinear Dyn. **87**(1), 633-646 (2017)
4. Zhou J., Wang X. L., Xu D. L., Bishop S.: Nonlinear dynamic characteristics of a quasi-zero stiffness vibration isolator with cam-roller-spring mechanisms. J Sound Vib. **346**, 53-69 **(**2015)
5. Wen J., Wang G., Yu D., Zhao H., Liu Y.: Theoretical and experimental investigation of flexural wave propagation in straight beams with periodic structures: Application to a vibration isolation structure. J. Appl. Phys. **97**(11), 114907 (2005)
6. Fok L., Ambati M., Zhang X.: Acoustic Metamaterials. MRS Bull. **33**(10), 931-934 (2008)
7. Ma G., Sheng P.: Acoustic metamaterials: From local resonances to broad horizons. Sci. Adv. **2**(2), e1501595 (2016)
8. Hussein M. I., Leamy M. J., Ruzzene M.: Dynamics of phononic materials and structures: Historical origins, recent progress, and future outlook. Appl. Mech. Rev. **66**(4), 040802 (2014)
9. Zhou X., Liu X., Hu G.: Elastic metamaterials with local resonances: an overview. Theor. Appl. Mech. Lett. **2**(4) , 041001 (2012)
10. Liu Z. Y., Zhang X. X., Mao Y. W., Zhu Y. Y., Yang Z. Y., Chan C. T., Sheng P.: Locally resonant sonic materials. Science. **289**(5485), 1734-1736 (2000)
11. Yu D. L., Liu Y., Wang G., Zhao H., Qiu J.: Flexural vibration band gaps in Timoshenko beams with locally resonant structures. J. Appl. Phys. **100**(12), 124901 (2006)
12. Yu D., Wen J., Shen H., Xiao Y., Wen X.: Propagation of flexural wave in periodic beam on elastic foundations. Phys. Lett. A **376**(4), 626-630 (2012)
13. Xiao Y., Wen J. H., Yu D. L., Wen X. S.: Flexural wave propagation in beams with periodically attached vibration absorbers: Band-gap behavior and band formation mechanisms. J. Sound Vib. **332**(4), 867-893 (2013)
14. Liu L., Hussein M. I.: Wave motion in periodic flexural beams and characterization of the transition between Bragg scattering and local resonance. J. Appl. Mech. **79**(1), 011003-17 (2011)
15. Zhu R., Liu X. N., Hu G. K., Sun C. T., Huang G. L.: A chiral elastic metamaterial beam for broadband vibration suppression. J. Sound Vib. **333**(10) , 2759-2773 (2014)
16. Wang X., Wang M.Y.: An analysis of flexural wave band gaps of locally resonant beams with continuum beam resonators. Meccanica **51**(1) , 171-178 (2016)
17. Xiao Y., Wen J. H., Wen X. S.: Broadband locally resonant beams containing multiple periodic arrays of attached resonators. Phys. Lett. A **376**(16), 1384-1390 (2012)
18. Krödel S., Thomé N., Daraio C.: Wide band-gap seismic metastructures. Extreme Mech. Lett. **4,** 111-117 (2015)
19. Chen Y., Hu G. K., Huang G. L.: A hybrid elastic metamaterial with negative mass density and

tunable bending stiffness. J. Mech. Phys. Solids **105**, 179-198 (2017)

20. Yilmaz C., Hulbert G. M., Kikuchi N.: Phononic band gaps induced by inertial amplification in periodic media, Phys. Rev. B **76**, 054309 (2007)
21. Yilmaz C., Hulbert G. M.: Theory of phononic gaps induced by inertial amplification in finite structures, Phys. Let. A **374**(34), 3576-3584 (2010)
22. Acar G., Yilmaz C.: Experimental and numerical evidence for the existence of wide and deep phononic gaps induced by inertial amplification in two-dimensional solid structures. J. Sound Vib. **332**(24), 6389-6404 (2013)
23. Yuksel O., Yilmaz C.: Shape optimization of phononic band gap structures incorporating inertial amplification mechanisms, J. Sound Vib. **355**, 232-245 (2015)
24. Taniker, S, Yilmaz, C.: Generating ultra wide vibration stop bands by a novel inertial amplification mechanism topology with flexure hinges. Int. J. Solids Struct. **106**, 129-138 (2017)
25. Frandsen N. M. M., Bilal O. R., Jensen J. S., Hussein M. I.: Inertial amplification of continuous structures: Large band gaps from small masses. J. Appl. Phys. **119**(12), 124902 (2016)
26. Barys M., Jensen, J. S., Frandsen N. M. M.: Efficient attenuation of beam vibrations by inertial amplification. Eur. J. Mech. A-Solid **71**, 245-257 (2018)
27. Li J., Li S.: Generating ultra wide low-frequency gap for transverse wave isolation via inertial amplification effects. Phys. Let. A **382** (5), 241-247 (2018)
28. Hou M., Wu J., Cao S., Guan D., Zhu Y.: Extremely low frequency band gaps of beam-like inertial amplification metamaterials. Mod Phys. Let. B **31**(27), 1750251 (2017)
29. Zhou J. X., Wang K., Xu D. L., Ouyang H. J.: Local resonator with high-static-low-dynamic stiffness for lowering band gaps of flexural wave in beams. J. Appl. Phys. **121**(4), 044902 (2017)
30. Zhou J. X., Wang K., Xu D. L., Ouyang H. J.: Multi-low-frequency flexural wave attenuation in Euler–Bernoulli beams using local resonators containing negative-stiffness mechanisms. Phys. Lett. A **381**(37), 3141-3148 (2017)
31. Vakakis A. F., King M. E., Pearlstein A. J.: Forced localization in a periodic chain of non-linear oscillators. Int. J. Nonlin. Mech. **29**(3), 429-447(1994)
32. Boechler N., Theocharis G., Job S., Kevrekidis P. G., Porter M. A., Daraio C.: Discrete breathers in one-dimensional diatomic granular crystals. Phys. Rev. Lett. **104**(24), 244302 (2009)
33. Boechler N., Theocharis G., Daraio C.: Bifurcation-based acoustic switching and rectification. Nat. Mater. **10**, 665 (2011)
34. Fang X., Wen J. H., Bonello B., Yin J., Yu D. L.: Ultra-low and ultra-broad-band nonlinear acoustic metamaterials. Nat. Commun. **8**(1), 1288 (2017).
35. Chakraborty G., Mallik A. K.: Dynamics of a weakly non-linear periodic chain. Int. J. Nonlin. Mech. **36**(2), 375-389 (2001)
36. Narisetti, R. K., Leamy M. J., Ruzzene M.: A perturbation approach for predicting wave propagation in one-dimensional nonlinear periodic structures. J. Vib. Acoust. **132**(3), 031001 (2010)
37. Manktelow K., Leamy M. J., Ruzzene M.: Multiple scales analysis of wave-wave interactions in a cubically nonlinear monoatomic chain. Nonlinear Dyna. **63**(1), 193-203 (2011)

38. Lazarov B. S., Jensen J. S.: Low-frequency band gaps in chains with attached non-linear oscillators. Int. J. Nonlin. Mech. **42**(10), 1186-1193 (2007)
39. Nayfeh, A. H., Mook D. T.: Nonlinear Oscillations. John Wiley & Sons, New York (1995)
40. Moon, F. C.: Chaotic Vibrations: An Introduction for Applied Scientists and Engineers. John Wiley & Sons, New York (1987)
41. Dai H.M., Ho K.M., Yang Z., Sheng P.: Non-periodic locally resonant sonic materials. The 14th International Congress on Sound and Vibration, Cairns, Australia, 9-12 July, 2007

Appendix A

The algebraic equations with respect to Θ_{p0}, Θ_{p1}, Θ_{p2} (p=1, 2, 3) and Y_{i0}, Y_{i1}, Y_{i2} (i=1, 2) are given by

$$
\begin{aligned}
&k_p\Theta_{p0}-\frac{1}{4}F_{d2}\omega^2W_p\left(x_1\right)\left(Y_{11}^4-2Y_{11}^2Y_{12}^2+Y_{12}^4\right)-\frac{1}{4}F_{d2}\omega^2W_p\left(x_2\right)\left(Y_{21}^4-2Y_{21}^2Y_{22}^2+Y_{22}^4\right)\\
&-W_p\left(x_1\right)\left(F_{s3}Y_{10}^3+F_{s1}Y_{10}\right)-W_p\left(x_2\right)\left(F_{s3}Y_{20}^3+F_{s1}Y_{20}\right)\\
&-\frac{1}{2}W_p\left(x_1\right)\left(Y_{11}^2+Y_{12}^2\right)\left[3F_{s3}Y_{10}+\omega^2\left(F_{d2}Y_{10}^2+F_{d1}Y_{10}+F_{d0}\right)\right]\\
&-\frac{1}{2}W_p\left(x_2\right)\left(Y_{21}^2+Y_{22}^2\right)\left[3F_{s3}Y_{20}+\omega^2\left(F_{d2}Y_{20}^2+F_{d1}Y_{20}+F_{d0}\right)\right]=0\qquad p=1,2,3
\end{aligned}
\tag{A.1-A.3}
$$

$$
\begin{aligned}
&k_p\Theta_{p1}-m_p\omega^2\Theta_{p1}-F_0W_p\left(0\right)+2\zeta_p\omega\sqrt{k_pm_p}\Theta_{p2}\\
&-\frac{1}{4}W_p\left(x_1\right)\left[\omega^2Y_{11}^2\left(2F_{d2}Y_{10}Y_{11}+F_{d1}Y_{11}\right)+3F_{s3}Y_{11}Y_{12}^2-2\omega^2Y_{11}Y_{12}\left(2F_{d2}Y_{10}Y_{12}+F_{d1}Y_{12}\right)\right]\\
&-\frac{1}{4}W_p\left(x_2\right)\left[\omega^2Y_{21}^2\left(2F_{d2}Y_{20}Y_{21}+F_{d1}Y_{21}\right)+3F_{s3}Y_{21}Y_{22}^2-2\omega^2Y_{21}Y_{22}\left(2F_{d2}Y_{20}Y_{22}+F_{d1}Y_{22}\right)\right]\\
&-\frac{3}{4}W_p\left(x_1\right)\left[F_{s3}Y_{11}^3+\omega^2Y_{12}^2\left(2F_{d2}Y_{10}Y_{11}+F_{d1}Y_{11}\right)\right]\\
&-\frac{3}{4}W_p\left(x_2\right)\left[F_{s3}Y_{21}^3+\omega^2Y_{22}^2\left(2F_{d2}Y_{20}Y_{21}+F_{d1}Y_{21}\right)\right]\\
&-W_p\left(x_1\right)\left[F_{s1}Y_{11}+3F_{s3}Y_{11}Y_{10}^2\right]-W_p\left(x_2\right)\left[F_{s1}Y_{21}+3F_{s3}Y_{21}Y_{20}^2\right]=0\qquad p=1,2,3
\end{aligned}
\tag{A.4-A.6}
$$

$$
\begin{aligned}
&k_p\Theta_{p2}-m_p\omega^2\Theta_{p2}-2\zeta_p\omega\sqrt{k_pm_p}\Theta_{p1}\\
&-\frac{1}{4}W_p\left(x_1\right)\left[\omega^2Y_{12}^2\left(2F_{d2}Y_{10}Y_{12}+F_{d1}Y_{12}\right)+3F_{s3}Y_{12}Y_{11}^2-2\omega^2Y_{11}Y_{12}\left(2F_{d2}Y_{10}Y_{11}+F_{d1}Y_{11}\right)\right]\\
&-\frac{1}{4}W_p\left(x_2\right)\left[\omega^2Y_{22}^2\left(2F_{d2}Y_{20}Y_{22}+F_{d1}Y_{22}\right)+3F_{s3}Y_{22}Y_{21}^2-2\omega^2Y_{21}Y_{22}\left(2F_{d2}Y_{20}Y_{21}+F_{d1}Y_{21}\right)\right]\\
&-\frac{3}{4}W_p\left(x_1\right)\left[F_{s3}Y_{12}^3+\omega^2Y_{11}^2\left(2F_{d2}Y_{10}Y_{12}+F_{d1}Y_{12}\right)\right]\\
&-\frac{3}{4}W_p\left(x_2\right)\left[F_{s3}Y_{22}^3+\omega^2Y_{21}^2\left(2F_{d2}Y_{20}Y_{22}+F_{d1}Y_{22}\right)\right]\\
&-W_p\left(x_1\right)\left[F_{s1}Y_{12}+3F_{s3}Y_{12}Y_{10}^2\right]-W_p\left(x_2\right)\left[F_{s1}Y_{22}+3F_{s3}Y_{22}Y_{20}^2\right]=0\qquad p=1,2,3
\end{aligned}
\tag{A.7-A.9}
$$

$$
\begin{aligned}
&F_{s1}Y_{i0}+F_{s3}Y_{i0}^3+\frac{1}{4}\omega^2F_{d2}\left(Y_{i1}^4+Y_{i2}^4\right)+\frac{3}{2}F_{s3}Y_{i0}\left(Y_{i1}^2+Y_{i2}^2\right)\\
&-\frac{1}{2}\omega^2Y_{i1}\left(\mathrm{M}_1Y_{i1}+2\mathrm{M}_2Y_{i0}Y_{i1}\right)-\frac{1}{2}\omega^2Y_{i2}\left(\mathrm{M}_1Y_{i2}+2\mathrm{M}_2Y_{i0}Y_{i2}\right)\\
&+\frac{1}{2}\omega^2\left(Y_{i1}^2+Y_{i2}^2\right)\left(F_{d2}Y_{i0}^2+F_{d1}Y_{i0}+F_{d0}\right)-\frac{1}{2}\omega^2F_{d2}Y_{i1}^2Y_{i2}^2=0\qquad i=1,2
\end{aligned}
\tag{A.10, A.11}
$$

$$F_{s1}Y_{i1}+\frac{3}{4}\left(F_{s3}-\omega^2\mathrm{M}_2\right)Y_{i1}^3-\left(\gamma+1\right)m_r\omega^2\left[\Theta_{11}W_1\left(x_i\right)+\Theta_{21}W_2\left(x_i\right)+\Theta_{31}W_3\left(x_i\right)\right]$$
$$+\frac{1}{4}\omega^2\left(Y_{i1}^2+3Y_{i2}^2\right)\left(F_{d1}Y_{i1}+2F_{d2}Y_{i0}Y_{i1}\right)-\omega^2Y_{i1}\left(\mathrm{M}_2Y_{i0}^2+\mathrm{M}_1Y_{i0}+\mathrm{M}_0\right) \qquad \text{(A.12, A.13)}$$
$$+\frac{3}{4}F_{s3}Y_{i1}\left(4Y_{i0}^2+Y_{i2}^2\right)-\frac{3}{4}\omega^2\mathrm{M}_2Y_{i1}Y_{i2}^2-\frac{1}{2}\omega^2Y_{i1}Y_{i2}\left(F_{d1}Y_{i2}+2F_{d2}Y_{i0}Y_{i2}\right)=0 \qquad i=1,2$$

$$F_{s1}Y_{i2}+\frac{3}{4}\left(F_{s3}-\omega^2\mathrm{M}_2\right)Y_{i2}^3-\left(\gamma+1\right)m_r\omega^2\left[\Theta_{12}W_1\left(x_i\right)+\Theta_{22}W_2\left(x_i\right)+\Theta_{32}W_3\left(x_i\right)\right]$$
$$+\frac{1}{4}\omega^2\left(Y_{i2}^2+3Y_{i1}^2\right)\left(F_{d1}Y_{i2}+2F_{d2}Y_{i0}Y_{i2}\right)-\omega^2Y_{i2}\left(\mathrm{M}_2Y_{i0}^2+\mathrm{M}_1Y_{i0}+\mathrm{M}_0\right) \qquad \text{(A.14, A.15)}$$
$$+\frac{3}{4}F_{s3}Y_{i2}\left(4Y_{i0}^2+Y_{i1}^2\right)-\frac{3}{4}\omega^2\mathrm{M}_2Y_{i2}Y_{i1}^2-\frac{1}{2}\omega^2Y_{i1}Y_{i2}\left(F_{d1}Y_{i1}+2F_{d2}Y_{i0}Y_{i1}\right)=0 \qquad i=1,2$$

where $x_1=L/3$, $x_2=2L/3$.